Light-Scattering Detection below the Level of Single Fluorescent Molecules for High-Resolution Characterization of Functional Nanoparticles

Shaobin Zhu,[†] Ling Ma,[†] Shuo Wang,[†] Chaoxiang Chen,[†] Wenqiang Zhang,[†]

Lingling Yang,[†] Wei Hang,[†] John P. Nolan,[‡] Lina Wu,[†] Xiaomei Yan[*,†]

[†] The MOE Key Laboratory of Spectrochemical Analysis & Instrumentation, The Key Laboratory for Chemical Biology of Fujian Province, Collaborative Innovation Center of Chemistry for Energy Materials, Department of Chemical Biology, College of Chemistry and Chemical Engineering, Xiamen University, Xiamen, Fujian 361005, P. R. China

[‡] The Scintillon Institute, 6404 Nancy Ridge Drive, San Diego, California 92121, USA

*To whom correspondence should be addressed. E-mail: xmyan@xmu.edu.cn

This PDF file includes the following:

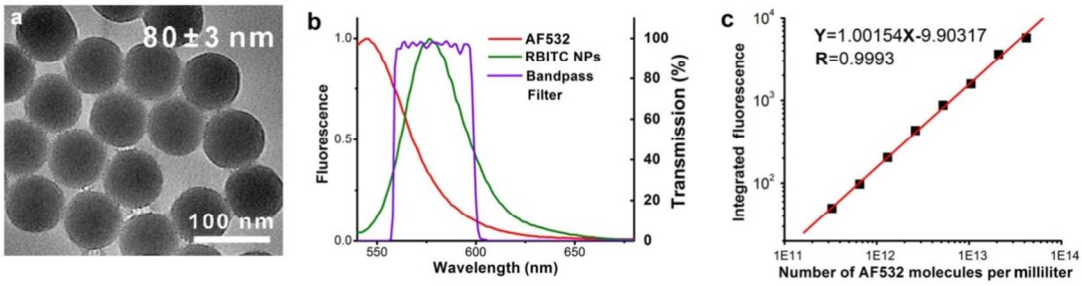

Supplementary Figure 1. Quantification of the fluorescence intensity of 80 nm fluorescent silica nanoparticles *via* spectrofluorometry. (a) TEM micrograph of 80-nm-diameter fluorescent silica nanoparticles. (b) Normalized emission spectra of Alexa Fluor 532 solution and RBITC-doped fluorescent silica nanoparticles (blank beads subtracted) and the transmission spectrum of the bandpass filter (FF01-579/34-25, Semrock) employed in the HSFCM setup. (c) Calibration curve constructed using standard solutions of Alexa Fluor 532.

Note: For consistency with the HSFCM setup, the integrated fluorescence within the transmission range of the bandpass filter was used in the fluorometric measurement for both the RBITC-doped fluorescent silica nanoparticles and the standard solutions of AF532. The spectral response of the spectrofluorometer components, *e.g.*, the gratings and PMT, in the 562–596 nm range is assumed to be uniform.

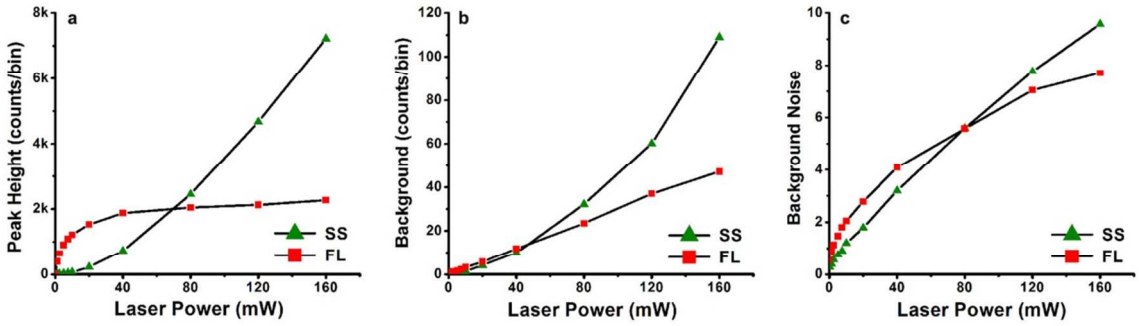

Supplementary Figure 2. Effect of the laser power on the side-scatter and fluorescence detection of single fluorescent nanoparticles. (a) Average peak height (background subtracted), (b) background, and (c) background noise of 80-nm-diameter fluorescent silica nanoparticles. Focused laser spot, 6.4 μm; ND filter on the SS channel, OD: 1.3 (20-fold).

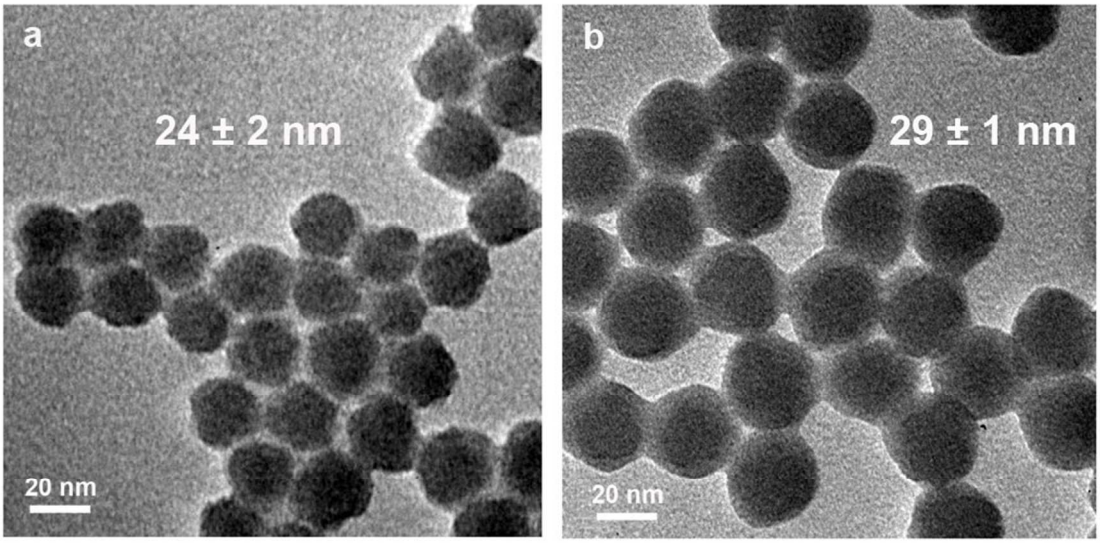

Supplementary Figure 3. TEM images of 24-nm-diameter and 29-nm-diameter silica nanoparticles.

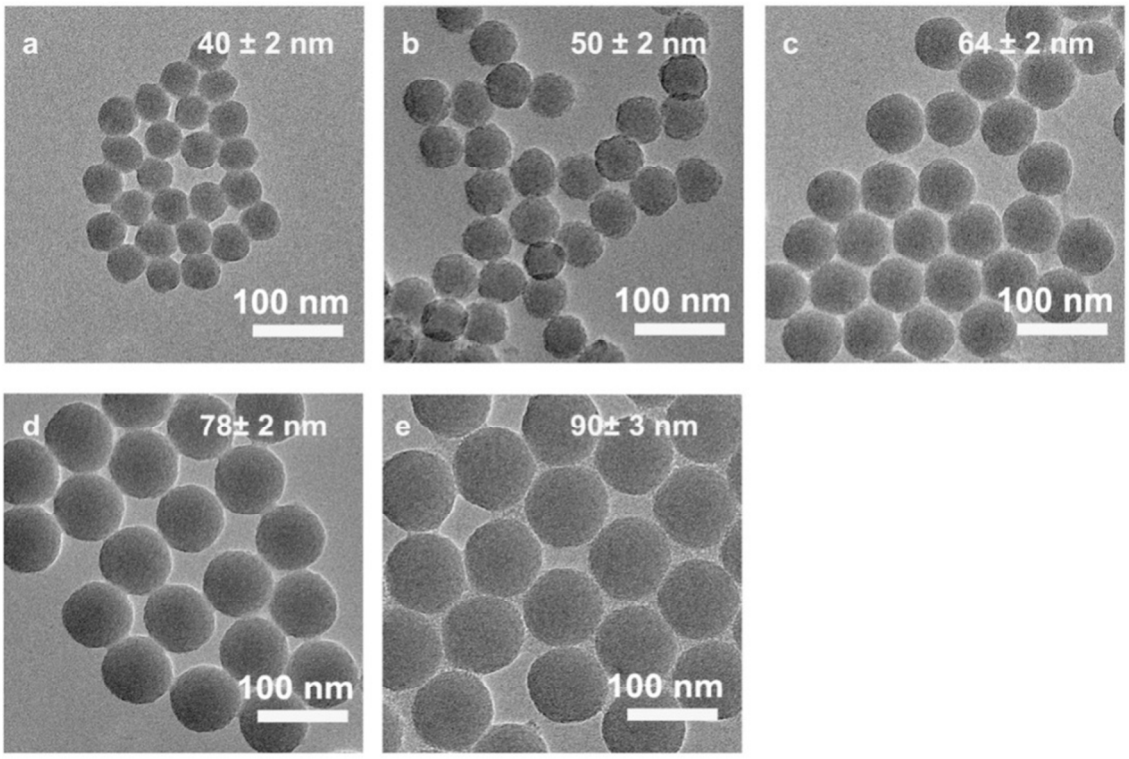

Supplementary Figure 4. TEM images of monodisperse silica nanoparticles of five different sizes ranging from 40 to 90 nm in diameter.

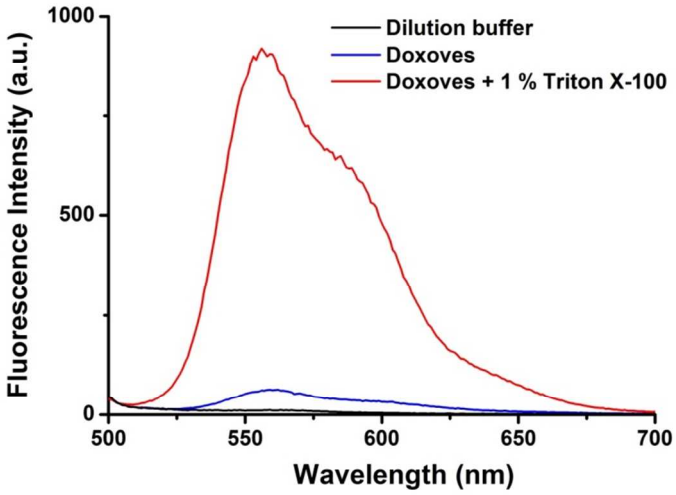

Supplementary Figure 5. Fluorescence-quenching measurement of liposome-encapsulated doxorubicin.

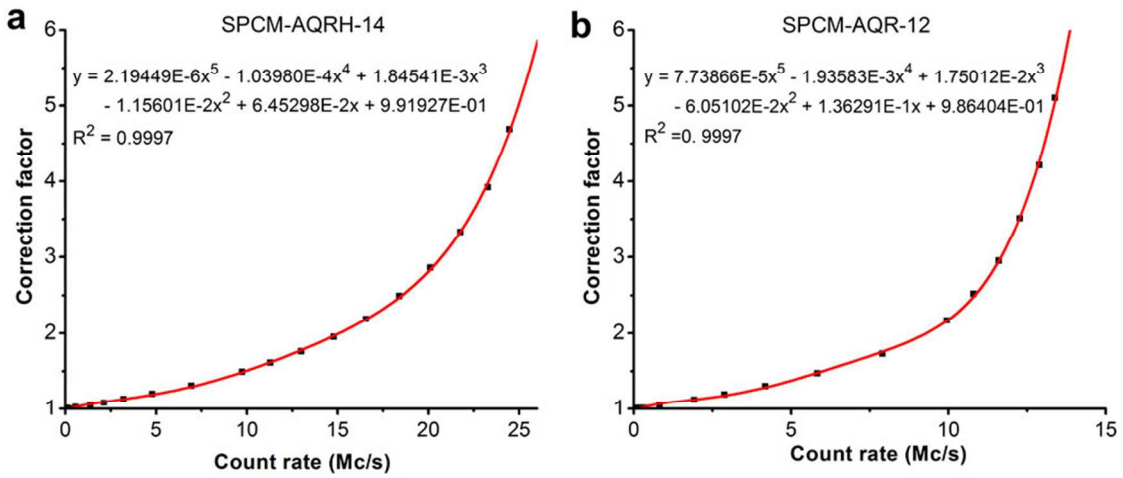

Supplementary Figure 6. APD count-rate-correction curves for SPCM-AQRH-14 (used for SS measurement) and SPCM-AQR-12 (used for FL measurement). A fifth-order polynomial curve was used to fit each detector's response curve to determine the correction coefficients.

S1: Materials and Chemicals

Spherical gold nanoparticles (AuNPs) of 6.7 nm (lot number JMW1106) and 10.4 nm (lot number JMW1043) in diameter were purchased from nanoComposix (San Diego, CA, USA). Orange FluoSpheres (100 nm in diameter) with excitation/emission maxima of 540/560 nm, SYTO 82 nucleic acid stains, and Alexa Fluor 532 were obtained from Molecular Probes (Eugene, OR, USA). Doxoves® Liposomal Doxorubicin HCl (catalogue # F30204B-D, batch # 04011301, drug concentration of 4.0 ± 0.05 mg/mL) was purchased from FormuMax Scientific, Inc. (Palo Alto, CA, USA). Highly monodisperse silica nanoparticles and fluorescent silica fluorescent nanoparticles were synthesized in accordance with the literature and resuspended in ethanol for further use.[1-3] All other reagents were obtained from Sinopharm Chemical Reagent Co., Ltd. (Shanghai, China) and were used as received unless stated otherwise. Distilled, deionized water (DI water), supplied by a Milli-Q RG unit, was used in the preparation of buffer solutions. All buffers and water were filtered through 0.22-μm filters (Millipore) prior to use.

S2: High-Sensitivity Flow Cytometry (HSFCM) Instrumentation

(S2-1): Laboratory-built HSFCM system. The system was designed to enable simultaneous measurement of the side-scatter (SS) and fluorescence (FL) signals emitted by nanoparticles passing individually through a tightly focused laser beam. A 200-mW, 532-nm continuous-wave solid-state Nd:YAG laser (Excelsior® 532, Spectra-Physics,

Santa Clara, CA, USA) was used as the excitation source. A half-wave plate and a polarizing beam splitter provided polarization control and continuously variable attenuation of the laser light. The laser excitation power was measured after the polarizing beam splitter, and 16 mW was used in the present study unless otherwise stated. The 0.34-mm laser output beam was focused to a spot with a diameter of approximately 16.0 μm ($1/e^2$) using an achromatic doublet lens with a 7.5-mm focal length onto the hydrodynamically focused sample stream inside a 250 μm × 250 μm square-bore quartz flow channel (NSG Precision Cells, Farmingdale, NY, USA). For the study of the effect of the laser power, the laser beam was focused to a spot with a diameter of approximately 6.4 μm ($1/e^2$) using a lens with a 3.1-mm focal length. The light emitted by individual nanoparticles was collected perpendicular to both the laser beam and the sample stream using an infinity-corrected microscopic objective (Olympus ULWD MSPlan 50×, 0.55 N.A.) and was then directed by a dichroic beam splitter (FF555-Di02, Semrock, Inc., Rochester, NY, USA) into two distinct light paths for SS and FL detection. The reflected light was spectrally filtered using a bandpass filter (FF01-524/24, Semrock, Inc.) to reduce the interference of fluorescence and was then focused by an aspheric lens onto a single-photon counting avalanche photodiode detector (APD, Excelitas Technologies model SPCM-AQRH-14, dark count 100 c/s) for SS detection. The transmitted light was spectrally filtered using a Raman edge filter (LP03-532RS, Semrock, Inc.) and a bandpass filter (FF01-579/34, Semrock, Inc.), and the light was then focused onto the second APD (Perkin Elmer SPCM-AQR-12, dark

count 500 c/s) by another aspheric lens for FL detection. The output signals from both APD detectors were simultaneously counted using a National Instruments DAQ card (PCIe-6321, Austin, TX, USA).

A custom program written in LabVIEW 2012 (National Instruments) was used for data acquisition and processing. In brief, the bin width was set to 100 μs, and the bursts of photons detected on both the SS and FL channels as nanoparticles passed individually through the laser beam were recorded simultaneously. For each sample, 1 min of data acquisition was performed. The running count-rate history data were dead-time corrected and then processed as follows: The threshold levels in both the peak height (a digital discriminator level set to 2–10 times the standard deviation of the background) and the peak width (0.1–0.3 ms) were used as the criteria for burst identification (both criteria can be interactively set by the user). For each burst that satisfied the criteria, the integrated number of photons detected was stored as the burst area. Although the small active area of the APD serves as a limiting aperture to minimize the light scattered outside the probed volume from reaching the detector, the background signal on the SS channel is always much stronger than that on the FL channel. A continuous background signal of approximately 200 counts/bin was constantly observed on the SS channel when the focused laser spot was 16 μm and the laser power was 16 mW. This background level increased to approximately 1800 counts/bin when the focused laser spot was 6.4 μm and the laser excitation power was 160 mW. This background signal was subtracted from the raw burst-trace data prior to burst-area integration and histogram construction.

(S2-2): APD dead-time correction. Following the detection of a photon, each APD has a characteristic dead time, a refractory period during which it is unresponsive. This dead-time interval sets the upper limit on the count rate and affects the performance of the unit in a statistical manner, hence the necessity for a dead-time-correction curve. For each APD detector, a fifth-order polynomial fitting was used to correlate the correction factor with the count rate (data provided by the manufacturer). The coefficients from the fit were stored in the file associated with each detector and used to "correct" or compensate for the dead time of the APD. Because of the sixth-order dependence of light scattering on particle size, it is important to choose an APD that can accommodate a wide range of count rates for SS detection to ensure a sufficiently large dynamic range when a mix of nanoparticles of large and small sizes is encountered. The SPCM-AQR-12 module used for the fluorescence detection in the present study is an older type of APD; the typical dead time is 50 ns, and the detector tends to saturate at count rates greater than 15 Mc/s. For the newly improved SPCM-AQRH single-photon-counting module (*e.g.*, SPCM-AQRH-14, which was used for SS detection in the present study), the typical dead time is 32 ns and the typical maximum count rate before saturation is 29 Mc/s. The count-rate-correction curves and the correction coefficients associated with these two APD detectors used in the present system are provided in Supplementary Figure 6. If a count rate of 28 Mc/s is encountered in the SS detection channel, the corresponding APD correction factor of 8.1 will result in a corrected count rate of 227 MHz. With a bin width of 100 μs, the burst height could reach 22.7k counts/bin. Therefore, even when

light-scatter bursts with peak heights of over 20k counts/bin were observed for 90-nm-diameter silica nanoparticles in the SS burst-trace data of Fig. 3a, the detected signal remained within the dynamic range of the SPCM-AQRH-14 detector.

(S2-3): HSFCM fluidics system. Sample fluidic was the same as that described before.[4,5] In brief, ultrapure water (Millipore, Bedford, MA, USA) filtered through 0.22-μm filters served as the sheath fluid *via* a gravity feed, and the flow rate was regulated by adjusting the relative height between the sheath supply bottle and the waste container. Under normal conditions, the measured sheath-flow rate was approximately 40 μL/min, as determined using an incremental method, resulting in an average linear flow velocity of 10.7 mm/s in the 250 μm × 250 μm flow cuvette. The square cuvette can be treated as a circular tube with the same cross section (radius: 141 μm).[6] Because the flow-velocity profile of a nearly laminar flow in a circular tube is parabolic in shape, the maximum sheath velocity in the center of the tube is approximately twice the average flow velocity, *i.e.*, 21.4 mm/s. The measured sample volumetric flow rate was approximately 2 nL/min as determined *via* calibration with a known concentration of 100-nm Orange FluoSpheres (Molecular Probes/Invitrogen). During hydrodynamic focusing, the sample stream was accelerated to the velocity of the sheath flow at the center, which resulted in particle transit times of 0.8 ms and 0.3 ms in the focused laser spots of 16 μm and 6.4 μm in diameter, respectively. To comply with the principle of mass conservation, the diameter

of the sample stream was reduced. Based on the flow rates of the sheath and sample streams, the diameter of the sample stream was approximately 1.4 μm as calculated using a relatively simple model developed by Dovichi *et al.*[6] Based on the overlap of the focused laser spot (approximately 16 μm or 6.4 μm) and the sample stream (approximately 1.4 μm in diameter), the calculated detection volumes (defined as the product of the size of the laser-beam spot and the sample-stream area) were approximately 25 fL or 10 fL, respectively. According to Poisson statistics, for a nanoparticle concentration of approximately 5×10^9/mL, the probability that two nanoparticles will pass through the probe volume (25 fL) simultaneously is 0.7%.

Because of the Gaussian profile of the focused laser beam (TEM_{00} mode), non-uniform illumination of the sample stream can result in broader SS and FL nanoparticle distributions depending on their trajectories through the laser beam. Numerical modeling performed by Dovichi *et al.*[7] has demonstrated that a monodisperse particle suspension will generate a light-scatter signal with a 2% relative standard deviation if the sample-stream radius is one-tenth the size of the laser-beam spot. In the present work, the sample stream radius (approximately 0.7 μm) was less than one-twentieth the size of the laser-beam spot (approximately 16 μm), such that uniform illumination of the nanoparticles was ensured regardless of their positions within the sample stream. Therefore, each nanoparticle flows through the apparatus at the same rate and experiences the same radiation field as it traverses the full width of the probed volume, thereby providing a foundation for the quantitative analysis of the physical and

chemical properties of single nanoparticles based on their scattering and fluorescence intensities.

In addition to the very small detection volumes (tens of femtoliters) produced and the uniform illumination of individual nanoparticles in the sample stream, there are several other distinct advantages to nanoparticle detection in a sheathed-flow system: 1) The sample stream is far from the cuvette windows and is surrounded by a sheath flow of pure water. The scattered light from the cuvette windows, which usually dominates the background in conventional instruments such as fluorometers, can be efficiently blocked by simple spatial masking.[8] 2) The sheath prevents particles in the core from coming into contact with the channel walls, thereby eliminating the contamination of the cuvette windows. 3) Hydrodynamic focusing permits the use of tubing with a large inner diameter for sample delivery, and clogging of the flow channel can be effectively avoided.

In conventional flow cytometry, the sensitive detection of submicron-sized particles in a sample can be hampered by background from impurity particles in the sheath fluid, even after filtration using standard 0.22-μm filters.[9] The number of background particles detected by a flow-cytometric system per unit time is determined by the interrogation region of the sheath stream (the region that is illuminated by the laser beam and sensed by the detector), the velocity of the sheath flow, and the concentration of impurity particles in the sheath fluid. The significantly reduced probe area of the sheath fluid and the much slower sheath-flow velocity (approximately 20 mm/s for HSFCM *versus*

approximately 6 m/s for conventional FCM) result in a significant reduction in the detected event rate of impurity particles in the sheath fluid by three to four orders of magnitude. Therefore, a much lower background can be achieved.

S3: Calculations

(S3-1): Calculations of the scattering cross section of single nanoparticles. For a spherical nanoparticle with a radius much smaller than the wavelength of the incident beam, the scattering cross section can be calculated as follows[10,11]:

$$\sigma_{scatt} = \frac{2\pi^5 d^6 n_{med}^4}{3\lambda^4} \left|\frac{m^2-1}{m^2+2}\right|^2, \qquad (1)$$

and

$$m = \frac{n_{particle}}{n_{med}} = \frac{n_{rel}+in_{im}}{n_{med}}, \qquad (2)$$

where d is the particle diameter, λ is the wavelength of the incident light, n_{med} is the refractive index of the medium surrounding the particle, and m is the ratio of the refractive indices of the particle ($n_{particle}$) and the medium (n_{med}). The refractive index m of a particle at a given wavelength is a complex number; n_{rel} and n_{im} are the real and imaginary parts of the index in vacuum, and $i = \sqrt{-1}$. The refractive index of the particle, $n_{particle}$, at a given wavelength is calculated using the refractive indices n_{rel} and n_{im} obtained from the literature[12] and assuming water as the solvent (n_{med} = 1.33). For silica nanoparticles with diameters of 24, 25, and 29 nm, the calculated scattering cross sections at 532 nm are 0.0063 nm^2, 0.0081 nm^2, and 0.020 nm^2, respectively.

(S3-2): Comparison of light-producing power between nanoparticles and fluorescent molecules. The absorption cross section σ_{abs} (cm^2) of a chromophore is directly related to the molar extinction coefficient ε ($M^{-1}cm^{-1}$) *via* the Avogadro constant (N_{av}):

$$\sigma_{abs} = 1000\, ln(10)\, \frac{\varepsilon}{N_{av}} = 2.303 \times 10^3\, \frac{\varepsilon}{N_{av}} = 3.82 \times 10^{-21}\, \varepsilon. \qquad (3)$$

For example, a molecule of fluorescein isothiocyanate (FITC) with a molar extinction coefficient of 68,000 $M^{-1}cm^{-1}$ at its maximum excitation wavelength of 494 nm corresponds to an absorption cross section of 2.6×10^{-16} cm^2 or 0.026 nm^2. The scattered light intensity of nanoparticles can be compared with that of fluorescent molecules using the following expression, which relates light-scattering cross section σ_{scatt} (cm^2) to the molar extinction coefficient ε ($M^{-1}cm^{-1}$) and fluorescence quantum yield ϕ_F of the fluorophores[13]:

$$\varepsilon\phi_F = \frac{\sigma_{scatt} N_{av}}{2.303 \times 10^3}. \qquad (4)$$

The equivalent $\varepsilon\phi_F$ of a 24-nm-diameter silica nanoparticle is 1.6×10^4 $M^{-1}cm^{-1}$. For Alexa Fluor 532, the reported ε and ϕ_F are 81,000 $M^{-1}cm^{-1}$ and 0.61, respectively, at the absorption maximum of 531 nm (Molecular Probes). Therefore, theoretically, the light-producing power of a 24-nm-diameter silica nanoparticle is equivalent to that of 0.3 Alexa Fluor 532 molecules.

(S3-3): Calculations of the laser excitation energy density and the number of photons emitted as a particle traverses the laser beam. The energy of a single photon at a wavelength of 532 nm can be calculated as follows:

$$E = h\nu = h\frac{C}{\lambda} = 6.626 \times 10^{-34} J \cdot s \times \frac{2.998 \times 10^{8} m \cdot s^{-1}}{5.32 \times 10^{-7} m} = 3.73 \times 10^{-19} J. \quad (5)$$

For a 532-nm CW laser with an excitation power of 160 mW, the number of photons emitted in one second can be calculated as follows:

$$N = \frac{0.160 J \cdot S^{-1} \times 1.00 s}{3.73 \times 10^{-19} J} = 4.29 \times 10^{17}\, photons/s, \quad (6)$$

With a laser focus spot of 6.4 μm in diameter, the excitation energy density is calculated as follows:

$$I = \frac{P}{A} = \frac{0.160 W}{3.14 \times 3.2^2 \times 10^{-8} cm^2} = 5.0 \times 10^{5}\, W/cm^2 \quad (7)$$

or

$$I = \frac{N}{A} = \frac{4.29 \times 10^{17} photons/s}{3.14 \times 3.2^2 \times 10^{-8} cm^2} = 1.3 \times 10^{24}\, photons/(s \cdot cm^2). \quad (8)$$

Therefore, for a 24-nm-diameter silica nanoparticle passing through the focused laser beam with a transit time of ~0.3 ms, the number of scattered photons can be estimated as follows:

$$n = \sigma_{scatt} I \cdot t =$$

$$0.0063 \times 10^{-14} cm^2 \times 1.3 \times 10^{24}\, photons/(s \cdot cm^2) \times 0.0003 s = 2 \times 10^{4} photons. \quad (9)$$

As described above, when the laser with an excitation power of 160 mW is focused to a 6.4-μm spot, the calculated laser excitation energy density is 5.0×10^5 W/cm^2. This density is on the same order of magnitude (MW/cm^2) as those used in most optical-tweezers experiments, in which the trapping laser beam is focused to a diffraction-limited spot using an objective of high NA to apply force to submicron

particles. Peterman *et. al.*[14] have reported that the temperature at the focus of the trapping beam increases by 7.7 ± 1.2 °C/W for 500-nm silica beads trapped in water. A laser power of 100 mW (at 1064 nm) causes a temperature increase of only ~0.8 °C at the focus. Because of the millisecond transit time of a nanoparticle through the focused laser beam, the photon-thermal damage to biological samples can be considered negligible in the HSFCM setup.

Supplementary References

1. Hartlen, K. D.; Athanasopoulos, A. P. & Kitaev, V. Facile Preparation of Highly Monodisperse Small Silica Spheres (15 to >200 Nm) Suitable for Colloidal Templating and Formation of Ordered Arrays. *Langmuir* **2008**, *24*, 1714-1720.

2. Wang, L. & Tan, W. Multicolor Fret Silica Nanoparticles by Single Wavelength Excitation. *Nano. Lett.* **2006**, *6*, 84-88.

3. Wu, C.; Zheng, J.; Huang, C.; Lai, J.; Li, S.; Chen, C. & Zhao, Y. Hybrid Silica-Nanocrystal-Organic Dye Superstructures as Post-Encoding Fluorescent Probes. *Angew. Chem. Int. Ed. Engl.* **2007**, *46*, 5393-5396.

4. Yang, L.; Zhu, S.; Hang, W.; Wu, L. & Yan, X. Development of an Ultrasensitive Dual-Channel Flow Cytometer for the Individual Analysis of Nanosized Particles and Biomolecules. *Anal. Chem.* **2009**, *81*, 2555-2563.

5. Zhu, S.; Yang, L.; Long, Y.; Gao, M.; Huang, T.; Hang, W. & Yan, X. Size Differentiation and Absolute Quantification of Gold Nanoparticles Via Single Particle Detection with a Laboratory-Built High-Sensitivity Flow Cytometer. *J. Am. Chem. Soc.* **2010**, *132*, 12176-12178.

6. Zarrin, F. & Dovichi, N. J. Sub-Picoliter Detection with the Shealth Floe Cuvette. *Anal. Chem.* **1985**, *57*, 2690-2692.

7. Zarrin, F. & Dovichi, N. J. Effect of Sample Stream Radius Upon Light Scatter Distributions Generated with a Gaussian Beam Light Source in the Sheath Flow Cuvette. *Anal. Chem.* **1987**, *59*, 846-850.

8. Zarrin, F.; Risfelt, J. A. & Dovichi, N. J. Light Scatter Detection within the Sheath Flow Cuvette for Size Determination of Multicomponent Submicrometer Particle Suspensions. *Anal. Chem.* **1987**, *59*, 850-854.

9. Steen, H. B. Flow Cytometer for Measurement of the Light Scattering of Viral and Other Submicroscopic Particles. *Cytometry A* **2004**, *57*, 94-99.

10. Bohren, C. F. & Huffman, D. R. *Absorption and Scattering of Light by Small Particles* (John Wiley & Sons, New York, 1983).

11. Yguerabide, J. & Yguerabide, E. E. Light-Scattering Submicroscopic Particles as Highly Fluorescent Analogs and Their Use as Tracer Labels in Clinical and Biological Applications. *Anal. Biochem.* **1998**, *262*, 137-156.

12. Berger, L. I. In *Crc Handbook of Chemistry and Physics* (eds D.R. Lide & H.P.R. Frederiske) 12-141-112-159 (CRC Press, 1994-1995).

13. Yguerabide, J. & Yguerabide, E. E. Light-Scattering Submicroscopic Particles as Highly Fluorescent Analogs and Their Use as Tracer Labels in Clinical and Biological Applications. *Anal. Biochem.* **1998**, *262*, 157-176.

14. Peterman, E. J.; Gittes, F. & Schmidt, C. F. Laser-Induced Heating in Optical Traps. *Biophys. J.* **2003**, *84*, 1308-1316.